Available online at www.sciencedirect.com
ScienceDirect
Trans. Nonferrous Met. Soc. China 34(2024) 361−377
Transactions of Nonferrous Metals Society of China
www.tnmsc.cn

Formation and characterization of $Al_{10}CaFe_2$ compound in Al−Ca−Fe alloys

N. A. BELOV[1], T. K. AKOPYAN[1,2], E. A. NAUMOVA[1],
V. V. DOROSHENKO[1], T. A. SVIRIDOVA[1], N. O. KOROTKOVA[1]

1. National University of Science and Technology MISIS, 4 Leninsky pr., Moscow 119049, Russia;
2. Baikov Institute of Metallurgy and Materials Science, 49 Leninsky pr., Moscow 119991, Russia

Received 9 August 2022; accepted 28 October 2022

Abstract: The phase diagram of the Al−Ca−Fe system in the aluminum corner, including the liquidus projection and solidification reactions, was studied by using thermodynamic calculations and experimental techniques. The results show that instead of the Al_3Fe phase, a ternary compound whose composition corresponds to the formula $Al_{10}CaFe_2$ should be in equilibrium with the aluminum solid solution (Al). The transition from the binary to the ternary compound occurs via the peritectic transformation L + Al_3Fe → (Al) + $Al_{10}CaFe_2$ (at 638 °C, 3.3 at.% Ca and 0.5 at.% Fe). Primary and eutectic crystals of the ternary compound have a compact morphology, in contrast to needle-shaped inclusions of the Al_3Fe phase. First principles calculations and X-ray diffraction analysis were used to determine the crystal lattice structure of $Al_{10}CaFe_2$ ternary compound. In addition, the near eutectic alloy Al−6wt.%Ca−1wt.%Fe after annealing at 500−600 °C has a fine structure with a total fraction of excess phases of about 25 vol.%. Thus, the Al−Ca−Fe system can be used to create new aluminum-matrix composite alloys.
Key words: Al−Ca alloys; intermetallic; phase diagram; phase transition; microstructure; aluminum-matrix composites

1 Introduction

The Al−Ca system is promising for the development of new generation casting and wrought aluminum alloys [1−5]. This system can be considered for the design of composite materials produced by additive manufacturing techniques [6]. Calcium, as well as silicon, forms a eutectic-type diagram with aluminum. The concentration of calcium in the binary eutectic is 7.4−7.6 wt.% and the corresponding temperature is 613−617 °C [7−9]. The distinctive feature of this eutectic is that the fraction of the second Al_4Ca phase exceeds 30 vol.%, which is three times that for the Al−Si eutectic. This allows one to achieve a special combination of various properties in the Al−Ca based alloys (eutectic composites). It was found in Ref. [10] that alloys based on the binary (Al) + Al_4Ca eutectic have high castability comparable to the Al−Si alloys. Despite the high fraction of the Al_4Ca phase, Al−Ca alloys have a sufficiently high deformation capacity making it possible to obtain rolled sheets and wires [3,5].

The design of alloys based on Al−Ca eutectics is significantly constrained by the limited information on multicomponent systems in the aluminum corner region. One of the most important systems is Al−Ca−Fe because it allows evaluating the effect of iron on the phase composition and system structure of Al−Ca alloys. It is well-known that the presence of iron as a harmful impurity is inevitable in most aluminum alloys [7]. The mechanical properties of castings and wrought semi-finished products (especially ductility) are largely dependent on the morphology of the Fe-

Corresponding author: N. A. BELOV, E-mail: nikolay-belov@yandex.ru
DOI: 10.1016/S1003-6326(23)66404-0

containing phases [2,11−23]. This is especially important in the preparation of alloys from recycled raw materials [24−29].

According to our previous work [5,30], in the aluminum corner of the Al−Ca−Fe system in addition to the known binary phases (Al_3Fe and Al_4Ca), iron and calcium form a ternary compound whose composition corresponds to the formula $Al_{10}CaFe_2$. This compound is absent from the databases, and its crystal lattice is unknown. According to the proposed structure of the Al−Ca−Fe phase diagram, the ternary compound can participate in two invariant reactions: eutectic ($L \rightarrow (Al) + Al_4Ca + Al_{10}CaFe_2$) and peritectic ($L + Al_3Fe \rightarrow (Al) + Al_{10}CaFe_2$). The former reaction is confirmed experimentally [30], while the latter one is hypothetical.

Based on the above, the main objectives of this work are identified as follows: (1) Define the parameters of the crystal lattice of the ternary compound using calculations and experimental techniques. (2) Confirm possible existence of the peritectic transformation and clarify the structure of the Al−Ca−Fe phase diagram in the aluminum corner.

2 Experimental

The experimental study was focused on six hypereutectic and one near-eutectic alloys of the Al−Ca−Fe system (see Table 1). The nominal compositions of these alloys were sufficiently close to the actual ones. Melting was carried out in an electric resistance furnace in a graphite−chamotte crucible. Experimental hypereutectic alloys with high Ca content (marked as 0.5Fe−4Fe) were prepared by mixing two binary master alloys (Al−15%Ca and Al−10%Fe). High purity grade aluminum (99.99%) was used for preparing the X and Y alloys. According to previously obtained results, the X alloy has the best structure among all the alloys of this ternary system containing 1 wt.% Fe [1,5,10]. The composition of the Y alloy was chosen based on the preliminary analysis, suggesting that an invariant peritectic transformation would occur in it. For achieving an equilibrium phase composition, some alloys were remelted and slowly solidified in the furnace chamber at a cooling rate of about 0.01 K/s.

The melt was poured into a graphite mold at ~800 °C in order to obtain flat ingots with dimensions of 10 mm × 20 mm × 150 mm (the cooling rate during solidification was ~15 K/s). The test samples were extracted from the obtained castings for studying the structure and properties.

Table 1 Nominal chemical compositions of experimental alloys

Designation	Ca content/wt.% (at.%)	Fe content/wt.% (at.%)	Al
0.5Fe	14.25(10.10)	0.50 (0.25)	Bal.
1Fe	13.50 (9.56)	1.00 (0.51)	Bal.
2Fe	12.00 (8.50)	2.00 (1.00)	Bal.
3Fe	10.50 (7.44)	3.00 (1.51)	Bal.
4Fe	9.00 (6.38)	4.00 (2.03)	Bal.
X	6.00 (4.14)	1.00 (0.50)	Bal.
Y	4.00 (2.77)	3.00 (1.49)	Bal.

The structure was examined using optical microscopy (OM, Axiovert 200 MMAT) and scanning electron microscopy (SEM, TESCAN VEGA 3) equipped with an electron microprobe analyzer (EMPA, Oxford Instruments, Aztec software). Polished samples cut from the central part of the ingots and sheets were studied. Mechanical polishing (Struers Labopol-5) was used, as well as electrolytic polishing, as these methods are complementary and enable the complete observation of the microstructure. Electrolytic polishing was carried out at 12 V in an electrolyte containing six parts ethanol, one part $HClO_4$ and one part glycerin.

Differential scanning calorimetry with a heating and cooling rate of 10 K/min was performed using a high temperature DSC Setaram Setsys Evolution. The experiment was carried out in a dynamic Ar atmosphere with a flow rate of 50 mL/min. A temperature accuracy of ±0.5 °C was obtained.

X-ray diffraction (XRD) data were collected in Cu K_α radiation and processed with software package [31]. The objects of the X-ray diffraction (XRD) study were polished specimens cut from part of the ingots. Based on the XRD data, the volume fraction and the lattice parameters of the phases were determined. The relative measurement error was 10% for the volume fractions and 0.15% for the lattice parameters.

The phase composition of the Al−Ca−Fe ternary system was calculated using Thermo-Calc software (TTAL5 database) [32].

To assess the crystal lattice structure of the $Al_{10}CaFe_2$ phase, first principles calculations based on the density functional theory (DFT) were carried out using Quantum ESPRESSO software based on Open-Source computer codes for electronic-structure calculations and material modeling at the nanoscale [33,34]. To obtain the initial input data for the calculation, the data on the crystal structure of the known compound $Al_{10}CeFe_2$ were used as follows. Cerium atoms were replaced with calcium atoms in the corresponding crystallographic information file (CIF) which was later used for the calculation. Further DFT calculations were aimed to find the ground state geometry of the obtained crystal. Based on the calculations, the data on the positions of the atoms and the shape of the unit cell (lattice parameters) for the new crystal were obtained. The Perdew–Burke–Ernzerhof (PBE) exchange-correlation functional together with the corresponding pseudopotential files for the Al, Fe and Ca atoms taken from Ref. [35] were used for the calculation. A three-dimensional grid in reciprocal space (k-mesh) and basis set size were chosen based on a series of tests, ensuring that the hydrostatic pressure on a given unit cell converges to about 100 MPa or better. The obtained theoretical crystal lattice data were further compared to the experimental XRD data.

3 Results

3.1 As-cast structure of hypereutectic alloys

The compositions of the hypereutectic alloys (see Table 1) were chosen to reveal the boundaries of the primary crystallization of intermetallic phases. Since the existing thermodynamic databases (including the one used by TTAL5) do not contain a description of the ternary compound, the calculated version shows the phase fields only with the Al_3Fe and Al_4Ca phases (Fig. 1(a)). As follows from the proposed phase distribution in the solid state (i.e. at the end of crystallization, see Fig. 1(b)), all the experimental alloys are in the (Al) + Al_4Ca + $Al_{10}CaFe_2$ phase region. However, due to the incompleteness of the peritectic transformation L + Al_3Fe → (Al) + $Al_{10}CaFe_2$ during nonequilibrium solidification, the structure of the alloys in the region of primary crystallization of the Al_3Fe phase inevitably contains this phase. The latter is well confirmed by the analysis results of their structure presented in Fig. 2.

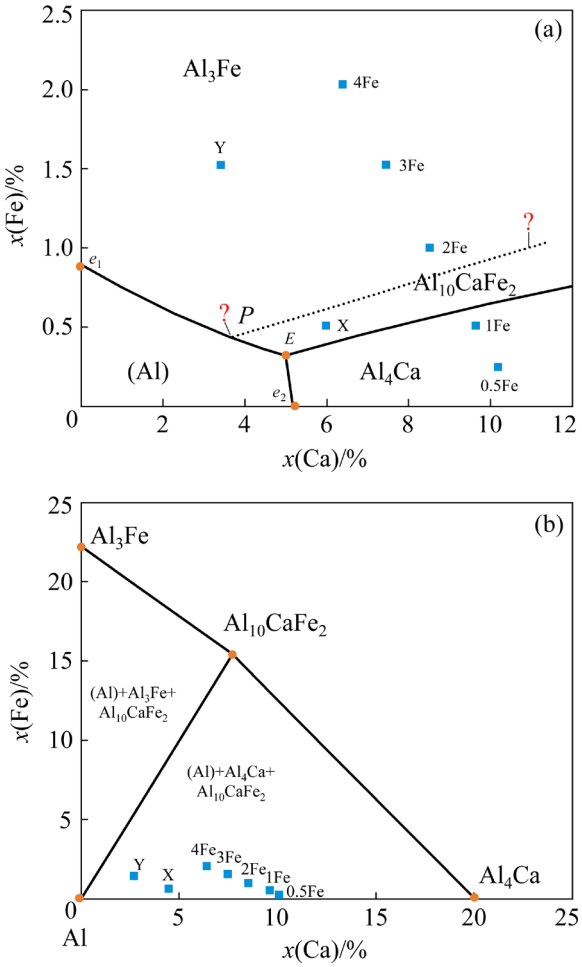

Fig. 1 Positions of experimental alloys on Al−Ca−Fe phase diagram: (a) Liquidus projection (calculated); (b) Proposed phase distribution in solid state

The structure of the alloy with the lowest iron content (0.5Fe), consists of a large number of primary Al_4Ca crystals, more than 100 μm in length and up to 50 μm in width (Fig. 2(a)). The eutectic has a fine fibrous structure, and the size of the constituent crystals does not exceed 2 μm. There are also compact white crystals enriched with iron, which allows one to identify them as $Al_{10}CaFe_2$.

In the 1Fe alloy, the primary crystals of the Al_4Ca phase may have a strictly elongated shape or a more branched or flaky structure (Fig. 2(b)). In addition, the structure of this alloy exhibits iron-containing particles (light in appearance) having a needle-like or compact shape. The former ones which do not contain calcium and have a length of

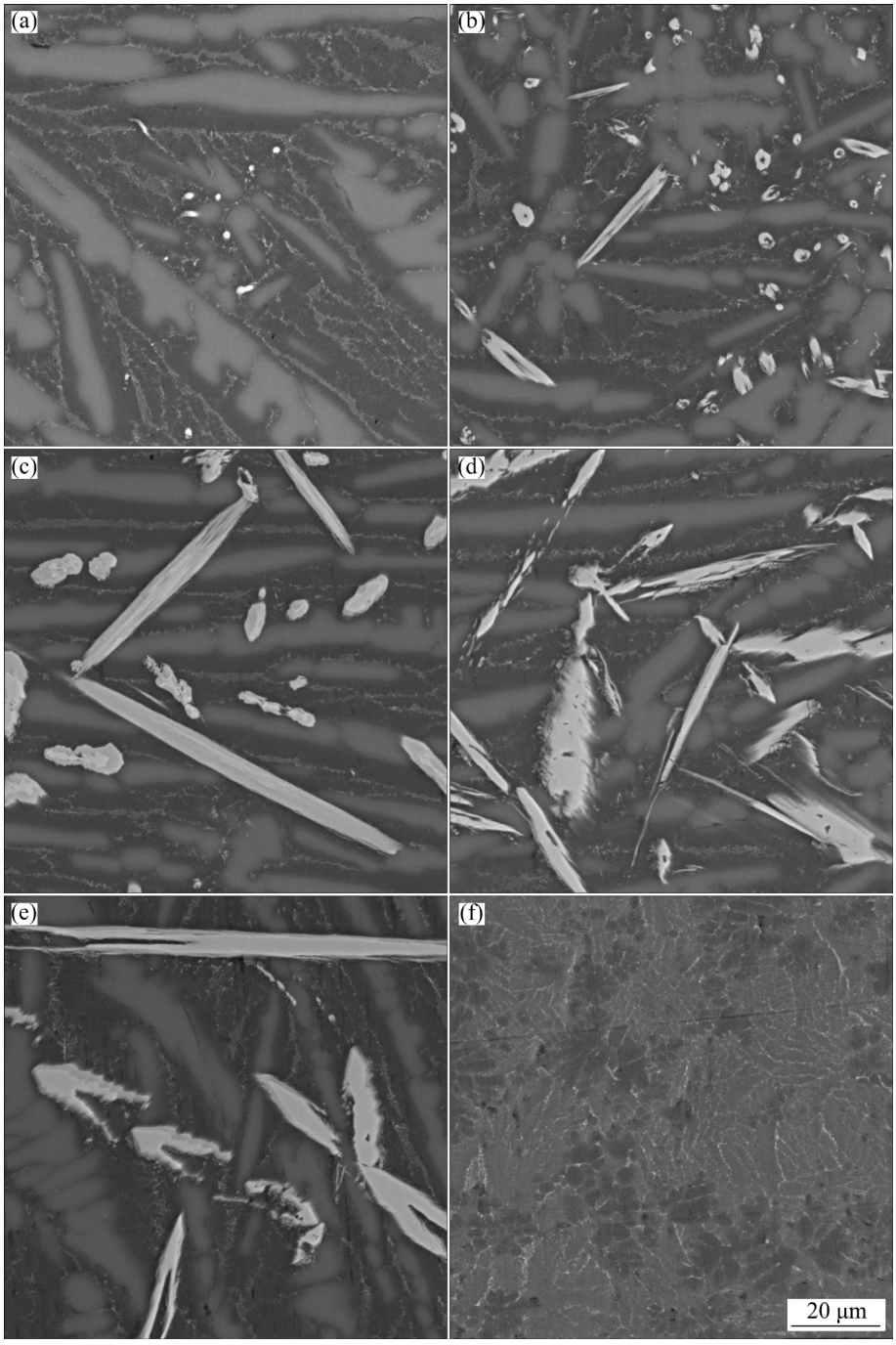

Fig. 2 SEM images of as-cast experimental alloys: (a) 0.5Fe; (b) 1Fe; (c) 2Fe; (d) 3Fe; (e) 4Fe; (f) X

up to 40 μm correspond to the Al_3Fe phase, and the latter ones, up to 10 μm in size, correspond to the ternary compound.

In high iron content alloys, an increase in the amount and size of the Al_3Fe phase is noticeable (Figs. 2(c−e)). Moreover, for some primary crystals of the Al_3Fe phase (Figs. 2(c) and (e)), one can also observe tiny gray rims which supposedly correspond to the ternary compound forming as a result of an incomplete peritectic transformation. In addition, according to the structural analysis data, with an increase in the iron content, thinning of the primary Al_4Ca crystals can be observed. In this case, the shape and size of the eutectic colonies do not change. The structure of the near-eutectic X alloy consists mainly of the fine eutectic with a small fraction of primary crystals (Al) (Fig. 2(f)). Primary crystals of intermetallic compounds, like those dominating in hypereutectic alloys (Figs. 2(a−e)), are absent.

Assuming that the accelerated cooling rate observed above should lead to substantial deviations in the structure compared to the equilibrium state (the peritectic transformation and primary crystallization of intermetallics can be partly or completely suppressed), the structure of slowly solidified alloys was also analyzed to confirm the presence of a peritectic transformation in the Al−Ca−Fe system. To obtain samples, weighed portions of initial ingots (20−30 g) were heated to above liquidus (50 °C) and held at this temperature for 1 h, and then cooled in the furnace. It follows from the results of the structural analysis that in the 0.5Fe alloy, the primary crystals are represented by only one phase Al_4Ca (Fig. 3(a)). The structure of the remaining hypereutectic alloys also includes needle-shaped Fe-containing particles (Figs. 3(b−e)). Among these particles (especially in

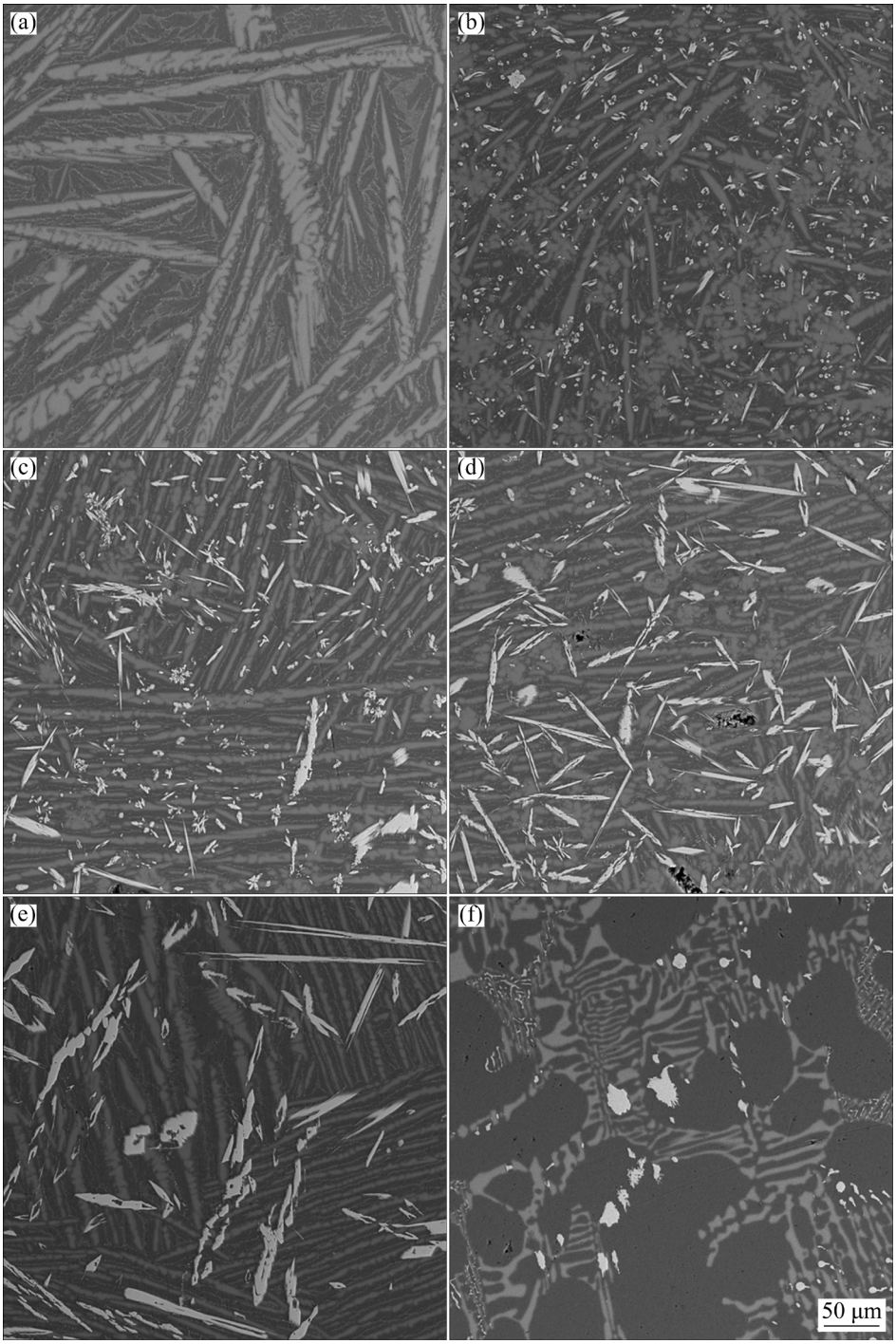

Fig. 3 SEM images of experimental alloys after slow solidification at ~0.1 °C/s: (a) 0.5Fe; (b) 1Fe; (c) 2Fe; (d) 3Fe; (e) 4Fe; (f) X

the 2Fe−4Fe alloys), there are many two-phase conglomerates consisting of light cores and gray rims. According to EMPA data, the composition of the cores corresponds to the Al_3Fe phase, and that of the rims corresponds to the $Al_{10}CaFe_2$ compound (Table 2).

In high iron content alloys, there are clear signs of a peritectic transformation which is clearly visualized by the element distribution maps. By way of example, Fig. 4 shows a typical section showing the 3Fe alloy with two-phase conglomerates consisting of light cores and gray rims. The cores do not contain calcium and represent the Al_3Fe phase, while the Ca-containing rims consist of the

Table 2 Chemical compositions of primary crystals in slowly solidified Al−Ca−Fe alloys

Alloy	Phase	Content/at.%			Content/wt.%		
		Ca	Fe	Al	Ca	Fe	Al
2Fe	Al_3Fe	0.04±0.04	23.26±0.35	76.30	0.05	38.42	61.53
	$Al_{10}CaFe_2$	7.76±0.04	14.57±0.04	77.66	9.67	25.17	65.16
	Al_4Ca	20.04±0.04	0.04±0.0.03	79.92	27.12	0.07	72.81
3Fe	Al_3Fe	0.03±0.01	23.33±0.23	76.64	0.04	38.52	61.44
	$Al_{10}CaFe_2$	7.74±0.10	14.58±0.29	77.68	9.64	25.19	65.17
	Al_4Ca	19.85±0.08	0.04±0.02	80.11	26.88	0.08	73.04
4Fe	Al_3Fe	0.04±0.01	22.41±0.08	77.45	0.05	37.29	62.66
	$Al_{10}CaFe_2$	7.76±0.11	14.25±0.05	77.99	9.70	24.69	65.61
	Al_4Ca	19.67±0.06	0.01±0.01	80.32	26.67	0.02	73.31

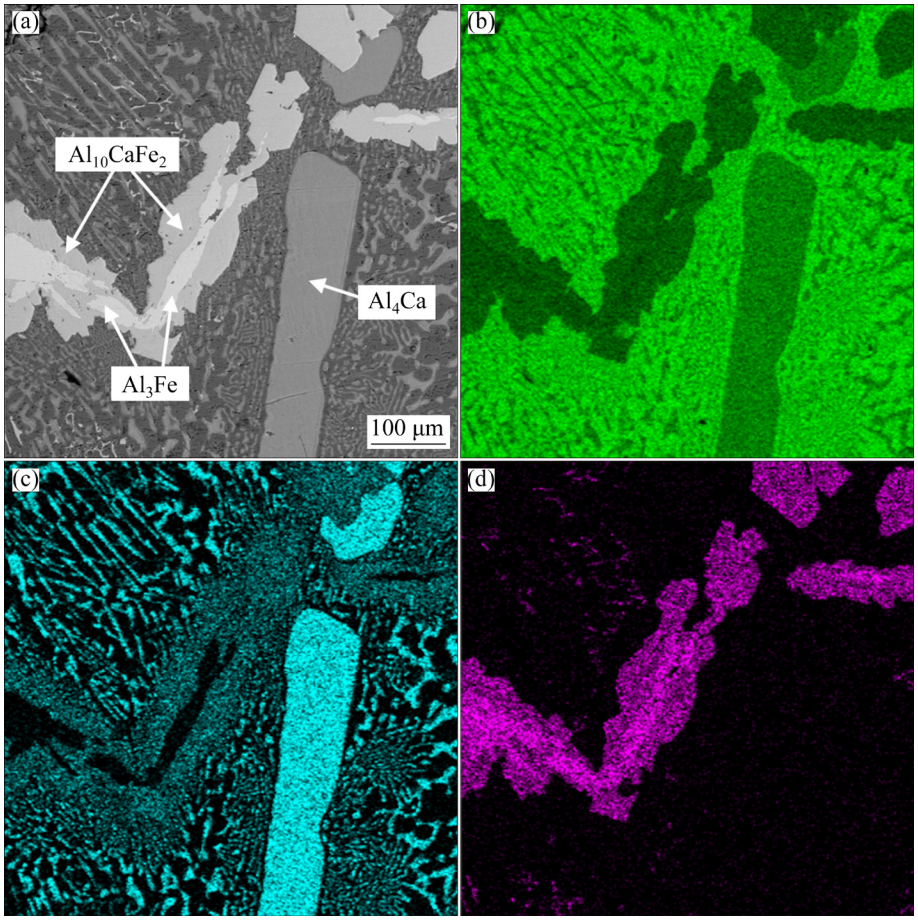

Fig. 4 SEM image (a) and corresponding EMPA mapping (b−c) of hypereutectic 3Fe alloy after slow solidification (~0.1 °C/s): (b) Al; (c) Ca; (d) Fe

$Al_{10}CaFe_2$ compound. A significant amount of large calcium aluminide crystals is also present in the structure. Since the initial Al_3Fe crystals with needle-like morphology occupy less than 30% of the total area of the conglomerate, one can assume that the peritectic transformation in this alloy has been largely completed.

In the 4Fe alloy, the fraction of the Al_3Fe phase primary crystals is the greatest in comparison with other alloys, and the crystals themselves are the largest (Fig. 3(e)). However, this alloy contains traces of a peritectic reaction, and the amount of the Al_4Ca phase is quite large (Fig. 3(e)). Thus, the structure of the 1Fe−4Fe alloys contains all the four phases considered and even after slow solidification it is far from equilibrium. On the other hand, no needle-shaped inclusions of the Al_3Fe phase were found in the structure of the near-eutectic X alloy (Fig. 3(f) and Fig. 5).

One should note that the average chemical compositions of all the large crystals of the ternary compound in the experimental alloys summarized in Table 2 are very close to each other and are quite close to the exact composition corresponding to the formula $Al_{10}CaFe_2$ (Table 2). The experimentally determined composition of the binary compounds is also quite close to earlier data [2,7]. In this case, the solubility of the third component in the binary compounds does not exceed 0.1%.

DSC curves of the 3Fe, Y and X alloys are shown in Fig. 6. Their common feature is the closeness of the solidus temperatures (about 611 °C), which corresponds to the eutectic reaction $L \rightarrow (Al) + Al_4Ca + Al_{10}CaFe_2$. The cooling curve of the 3Fe alloy shows high-temperature peaks at 758 and 677 °C (Fig. 6(a)). The former is associated with the formation of primary crystals of Al_3Fe phase (i.e., this is liquidus), and the latter, with the onset of the monovariant peritectic transformation $L + Al_3Fe \rightarrow Al_{10}CaFe_2$. The cooling curve of the Y alloy after a small peak associated with the formation of primary Al_3Fe phase crystals reveals two strong thermal effects (Fig. 6(b)), which can be associated with the invariant peritectic and eutectic

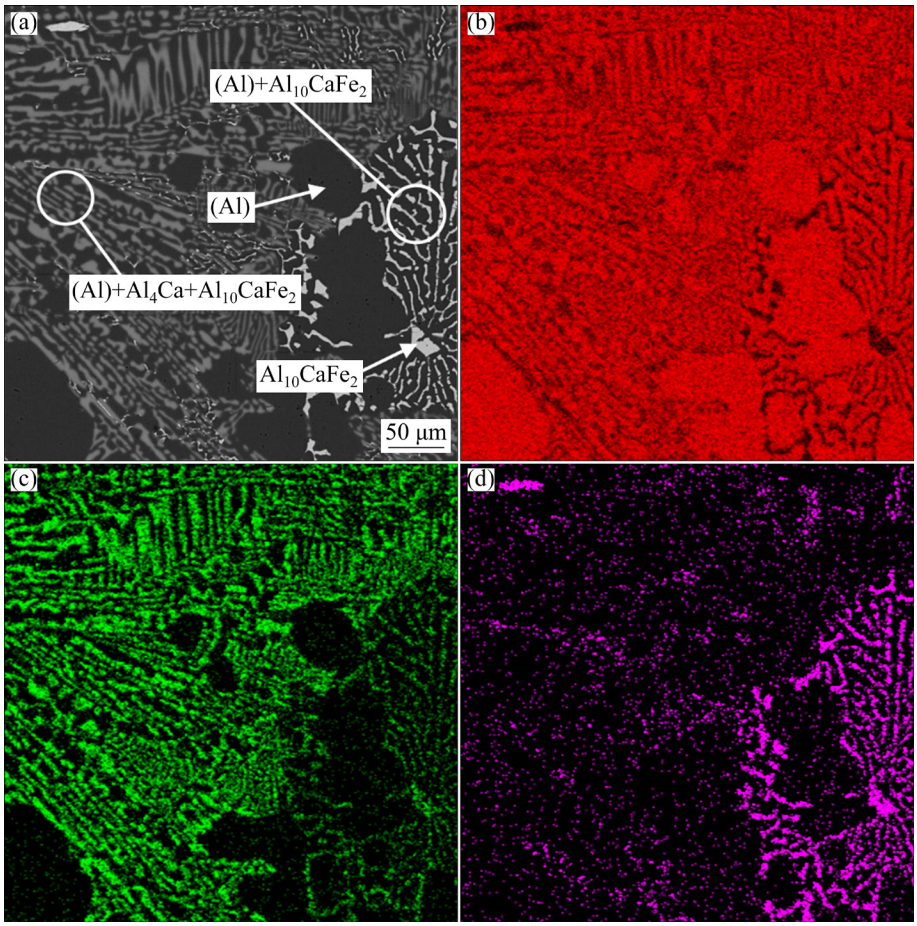

Fig. 5 SEM image (a) and EMPA mapping (b−d) of near-eutectic X alloy after slow solidification (~0.1 °C/s): (b) Al; (c) Ca; (d) Fe

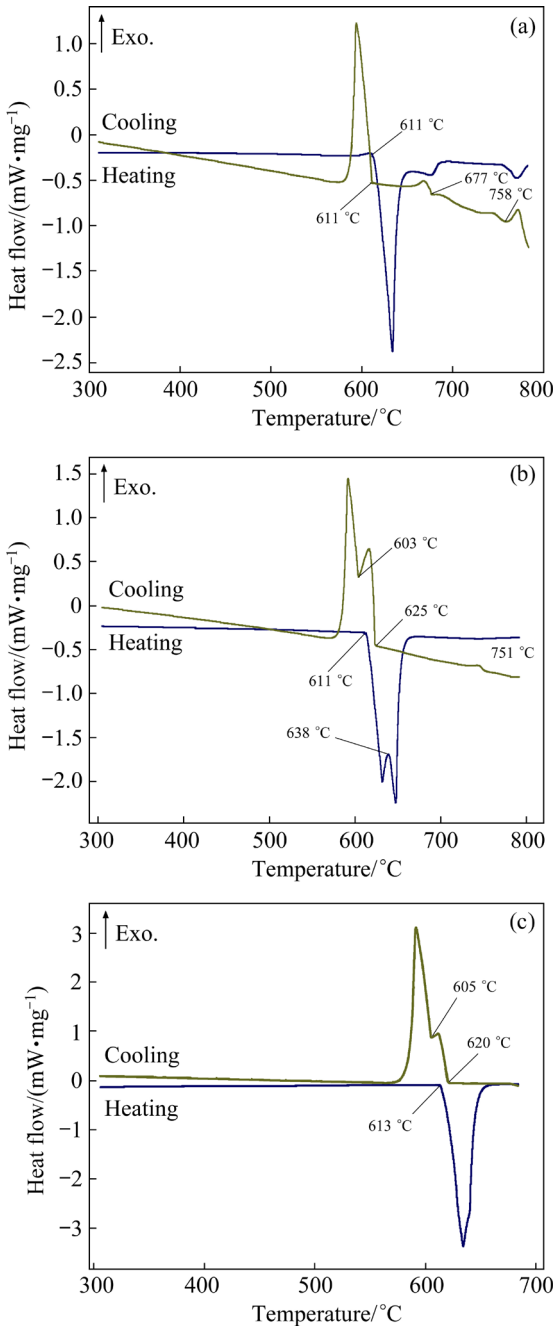

Fig. 6 DSC heating and cooling curves of hyper-eutectic alloys: (a) 3Fe; (b) Y; (c) Near-eutectic X alloy

reactions. The heating curve also shows two strong thermal effects at 611 and 638 °C. Since these effects are related to the heat absorption, it is likely that a significant amount of aluminum melts at these temperatures. DSC curves of near-eutectic X alloy are the simplest (Fig. 6(c)), since the solidification range for this alloy is the narrowest and the Al_3Fe phase is not formed in it (see Fig. 3(f)).

Based on the obtained DSC data for the Y alloy, one can assume that the invariant peritectic transformation (L + Al_3Fe → (Al) + $Al_{10}CaFe_2$) should take place in this alloy at temperatures of 625−638 °C. To confirm this assumption, the structure of the Y alloy was studied under different solidification conditions, e.g. after preliminary 3 h exposure (followed by quenching in water) in a solid−liquid state at temperatures slightly higher (647 °C) and lower (623 °C) than the above-mentioned range. The as-cast microstructure of the Y alloy contains primary crystals of the Al_3Fe phase (Fig. 7(a)), corresponding to the calculated variant of the liquidus surface (Fig. 1(a)). From Fig. 7(b), one can observe that during 623 °C temperature exposure, instead of needle-shaped crystals of the Al_3Fe phase (Figs. 7(a, d, g)), compact morphology inclusions of the ternary compound are formed (Figs. 7(b, e, h)). This change in the microstructure indicates that at this temperature the alloy is in the L + (Al) + $Al_{10}CaFe_2$ phase region, and the temperature of the invariant peritectic transformation is higher than 623 °C. At a higher exposure temperature, large crystals of the Al_3Fe compound are clearly visible against the quenched liquid background, and crystals of the ternary compound are absent (Figs. 7(c, f, i)). This suggests that the temperature of the invariant peritectic transformation is lower than 647 °C.

3.2 Modeling of crystal lattice

Analysis of the literature revealed that the ternary Al−Ce−Fe [36−39], Al−La−Fe [39−41] and Al−Nd−Fe [39,42] systems contain some compounds, which can be used as a basis for describing the new ternary $Al_{10}CaFe_2$ compound found in the Al−Ca−Fe system. As can be seen from Table 3, two types of compounds can be in equilibrium with aluminum in these systems. Most of publications [36−38,40−42] report the compound based on the formula Al_8ReFe_4 (Re is a rare earth metal) with a tetragonal space group (*I*4/*mmm*) and $ThMn_{12}$ structure type. However, there is also the publication [39] on the $Al_{10}ReFe_2$ compound with an orthorhombic space group (*Cmcm*) and $YbFe_2Al_{10}$ structure type. Since the chemical composition of the latter compound best matches the new $Al_{10}CaFe_2$ compound, its structure was taken as the basis for the DFT calculation. Cerium atoms were replaced with calcium atoms in the corresponding CIF which was later used for the calculation. Further DFT calculations were

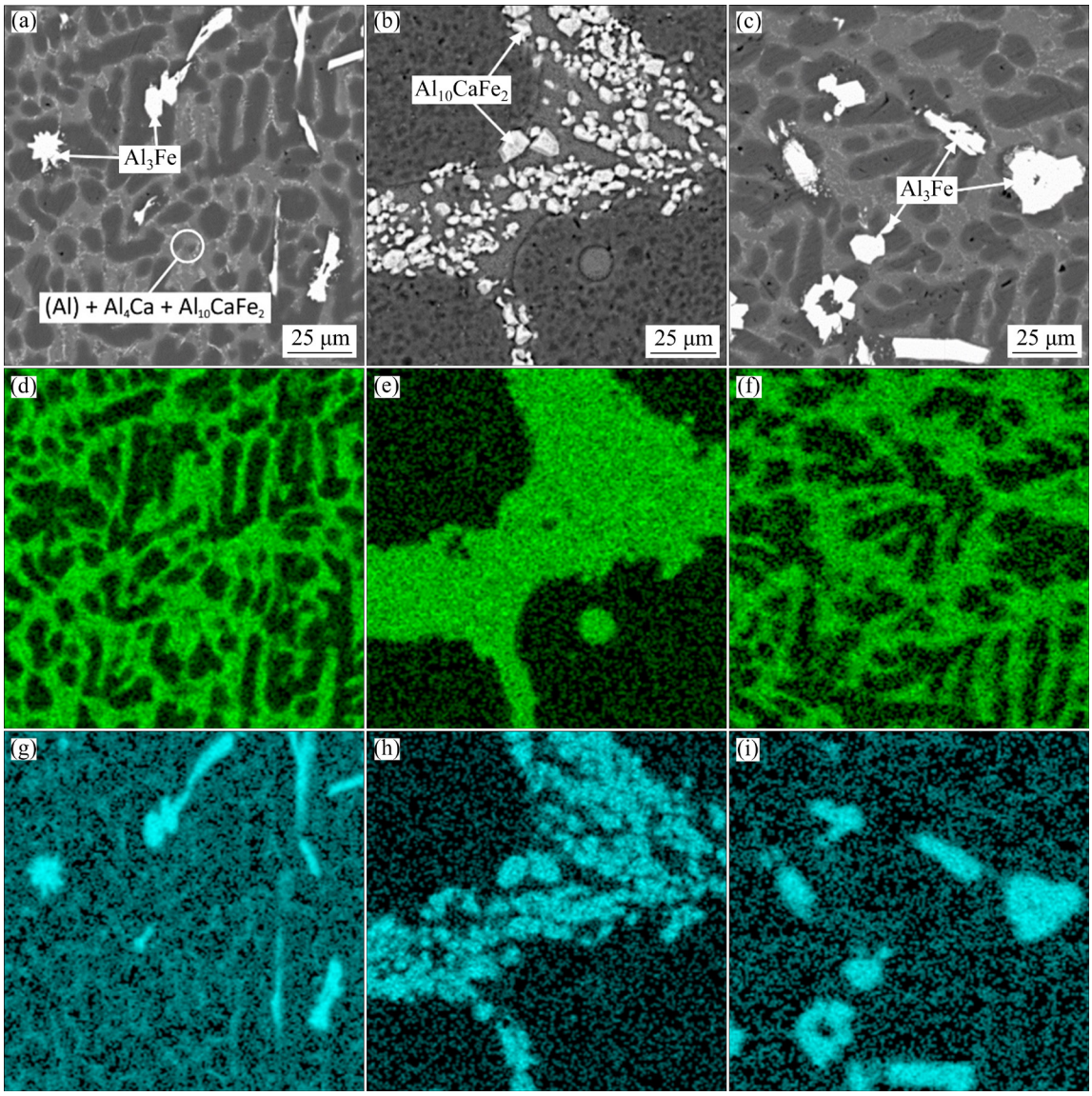

Fig. 7 SEM images (a−c) and EMPA mapping (d−i) of hypereutectic Y alloy: (a, d, g) As-cast state; (b, e, h) After 3 h holding at 623 °C; (c, f, i) After 3 h holding at 647 °C; (d, e, f) Ca; (g, h, i) Fe

aimed to find the ground state geometry of the obtained crystals. Based on the calculations, data on the positions of the atoms and the unit cell shape (Fig. 8) and lattice parameters (a=8.964 Å, b=10.174 Å, c=8.911 Å) for the new crystal were obtained. It can be seen that the lattice parameters obtained are close to those for all $Al_{10}ReFe_2$ type compounds (Table 3).

3.3 XRD analysis

For experimental confirmation of the data on the crystal lattice of the new $Al_{10}CaFe_2$ compound obtained using DFT, XRD analysis of a special sample prepared from the 3Fe alloy was performed. However, the maximum possible fraction of the $Al_{10}CaFe_2$ phase is ~ 10 vol.% which is insufficient to reliably identify a new compound. To increase the fraction of the ternary compound, the alloy was heated to 620 °C (i.e. slightly above the solidus, see Fig. 7(a)) and after 3 h exposure was cooled in water. One can assume that during the exposure, the formation of a phase composition close to equilibrium (i.e., L + Al_4Ca + $Al_{10}CaFe_2$) is possible, and primary crystals which have a higher density compared to liquid aluminum can settle to the bottom of the crucible. As one can see from Fig. 9, the structure of the sample thus obtained contains needle-shaped crystals of two phases the composition of which, as expected, corresponds to Al_4Ca and $Al_{10}CaFe_2$ (i.e., iron is completely included in the ternary compound).

Table 3 Crystal lattice parameters of some ternary compounds in Al−Fe−X system

System	Compound	Composition/ wt.%	Space group	Structure type	Pearson symbol	Atomic volume/nm^3	Density/ (g·cm^{-3})	Ref.
Al−Fe−Ce	Al_8CeFe_4	24.2 Ce, 38.5 Fe	*I*4/*mmm*, *a*=(8.82−8.86) Å, *c*=(5.06−5.08) Å	$ThMn_{12}$	tI26	15.16−15.34	4.90	[36−38]
	$Al_{10}CeFe_2$	26.8 Ce, 21.4 Fe	*Cmcm*, *a*=9.002 Å, *b*=10.222 Å, *c*=9.073 Å	$YbFe_2Al_{10}$	oC52	16.05	4.20	[39]
Al−Fe−La	Al_8LaFe_4	24La, 38.5Fe	*I*4/*mmm*, *a*=8.85−8.94 Å, *c*=5.05−5.08 Å	$ThMn_{12}$	tI26	15.24-15.60	4.85	[40,41]
	$Al_{10}LaFe_2$	27 La, 21.5 Fe	*Cmcm*, *a*=9.051 Å, *b*=10.249 Å, *c*=9.122 Å	$YbFe_2Al_{10}$	oC52	16.27	4.08	[39]
Al−Fe−Nd	Al_8NdFe_4	24.7 Nd, 38.2 Fe	*I*4/*mmm*, *a*=8.81 Å, *b*=8.81 Å, *c*=5.08 Å	$ThMn_{12}$	tI26	15.17	4.93	[42]
	$Al_{10}NdFe_2$	27.4 Nd, 21.2 Fe	*Cmcm*, *a*=9.006, *b*=10.206, *c*=9.069	$YbFe_2Al_{10}$	oC52	16.03	4.20	[39]

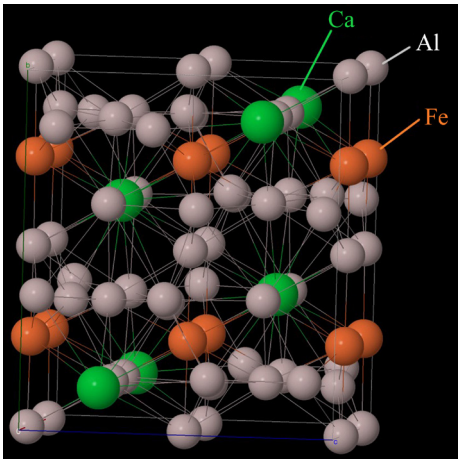

Fig. 8 Visualization of DFT calculated crystal lattice of $Al_{10}CaFe_2$ compound (Visualization was made in Jmol program)

The XRD analysis well confirms the existence of both compounds (Fig. 10) and allows one to identify the lattice structure of the new $Al_{10}CaFe_2$ compound. One should note that the theoretical determination of lattice parameters made in the manner described above allows one to estimate, in the first approximation, the crystal structure of an unknown compound (Table 4).

4 Discussion

4.1 Description of Al−Ca−Fe phase diagram in aluminum corner

The experimental results presented above allows one to suggest the presence of the invariant peritectic transformation L + Al_3Fe → (Al) + $Al_{10}CaFe_2$ in the ternary system considered. This is consistent with the structure of many other ternary systems Al−Fe−X [15,16,19,43]. In particular, in the Al−Fe−Si [19,43], Al−Fe−Ni [19,43], Al−Fe−Ni [15,16] and Al−Fe−Ce [2] systems, there are similar reactions involving the Al_3Fe phase, which are summarized in Table 5. A common feature of these systems is the wide region of primary crystallization of the Al_3Fe phase. Since the peritectic transformation proceeds only partially even during slow solidification, the structure of most ternary alloys, as a rule, contains Al_3Fe inclusions. The latter is undesirable since they have a negative effect on most mechanical properties, in particular ductility, fracture toughness, and fatigue strength [2,7]. According to the previous

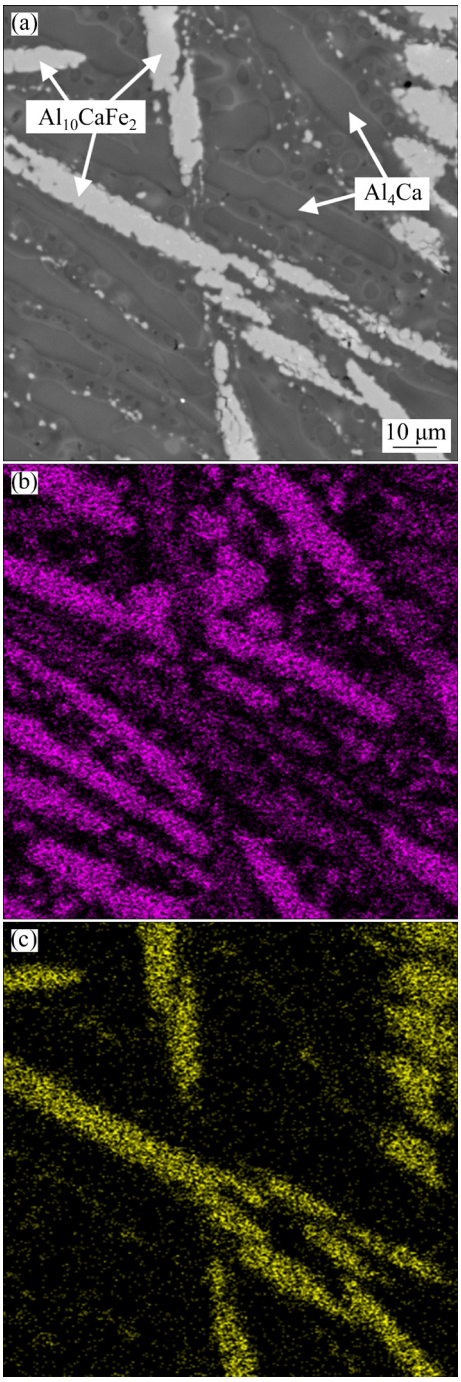

Fig. 9 SEM image (a) and EMPA mapping (b, c) of 3Fe alloy after 3 h exposure at 620 °C (above solidus): (b) Ca; (c) Fe

calculations of multicomponent Ca-containing alloys with the Thermo-Calc software (the TTAL5 database) despite the absence of ternary Ca-containing compounds, it allows a fairly accurate estimation of the liquidus (T_L) and solidus (T_S) temperatures [1]. Therefore, the corresponding calculations were carried out for the experimental alloys considered in this work (Table 1).

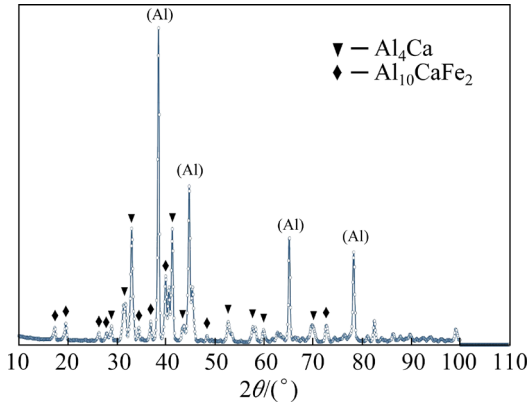

Fig. 10 XRD pattern of 3Fe alloy

Table 4 Quantitative data on phase composition of Al−10.5Ca−3Fe alloy obtained by XRD

Phase	Pearson symbol	Volume fraction/%	Lattice parameter/Å
(Al)	cF4/1	51.8±0.1	a=4.048
Al_4Ca	tI10/1	26.6±0.1	a=4.370, c=11.247
$Al_{10}CaFe_2$	oC52/14	21.6±0.1	a=9.024, b=10.200, c=9.062

Table 5 Peritectic reactions with Al_3Fe phase in Al−Fe−X systems [2,15,16,19,43]

System	Reaction	Composition of liquid/at.% (wt.%)		T/°C
		Fe	X	
Al−Fe−Si	L + Al_3Fe → (Al) + Al_8Fe_2Si	1.0 (2.0)	3.9 (4.0) Si	629
Al−Fe−Cu	L + Al_3Fe → (Al) + $(Al,Cu)_6Fe$	0.7 (1.4)	4.9 (10.8) Cu	620
Al−Fe−Ni	L + Al_3Fe → (Al) + Al_9FeNi	0.8 (1.7)	0.8 (1.7) Ni	649
Al−Fe−Ce	L + Al_3Fe → (Al) + $Al_{10}CeFe_2$	1.0 (2.0)	0.5 (2.5)*	650

*The content of cerium appears to be underestimated

According to the calculated dependence of the mass fraction of solid phases (f_s) versus temperature (Sheil−Gulliver simulation) given in Fig. 11, the T_L values are 706, 697, 740, 786 and 802 °C for the 0.5Fe, 1Fe, 2Fe, 3Fe and 4Fe hypereutectic alloys, respectively. For the 0.5Fe and 1Fe alloys, crystallization should begin with the formation of the Al_4Ca phase (Figs. 11(a, b)), and for others, with the Al_3Fe phase (Figs. 11(c−e)). This character of crystallization is consistent with the structures of

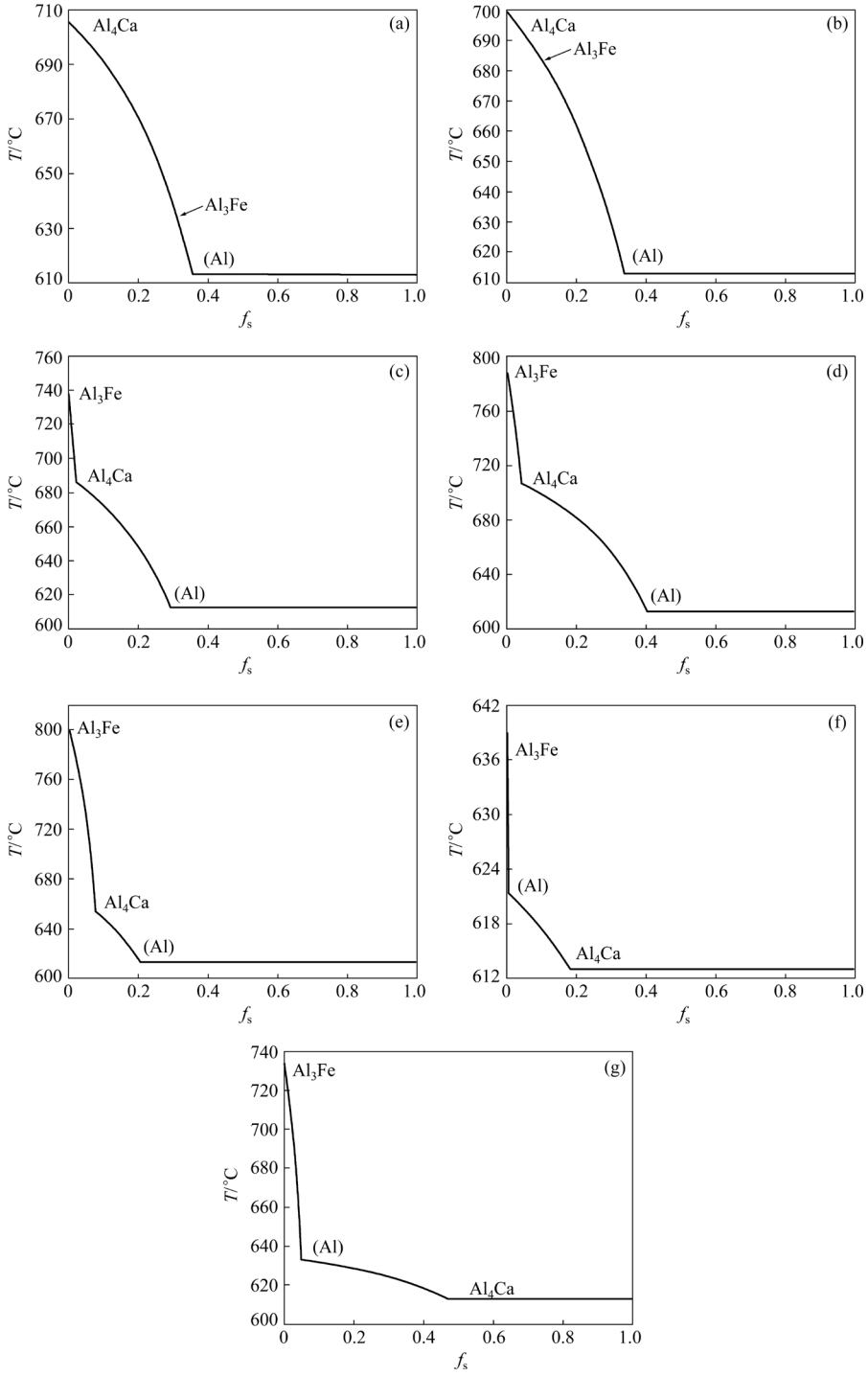

Fig. 11 Calculated dependence of mass fraction of solid phases (f_s) on temperature (Sheil−Gulliver simulation) for experimental alloys: (a) 0.5Fe; (b) 1Fe; (c) 2Fe; (d) 3Fe; (e) 4Fe; (f) X; (g) Y

all slowly cooled alloys, except for 1Fe alloy. The presence of the Al_3Fe phase in the structure of the 1Fe alloy (Fig. 3(b)) and its absence in the 0.5Fe alloy (Fig. 3(a)) means that the region of primary crystallization of the $Al_{10}CaFe_2$ compound is rather narrow, as shown in Fig. 12(a) (between the lines *Pm* and *En*). In the X and Y alloys, crystallization must also begin with the formation of the Al_3Fe compound (Figs. 11(f, g)). However, unlike alloys with a high calcium content (Figs. 11(a−e)), the Al_4Ca compound is formed in these alloys only during the invariant eutectic reaction (i.e., at the end of solidification). One should note that according to Fig. 11(f), the amount of the Al_3Fe phase in the X alloy is very small, and after slow solidification it is not detected in the microstructure (Fig. 5). The

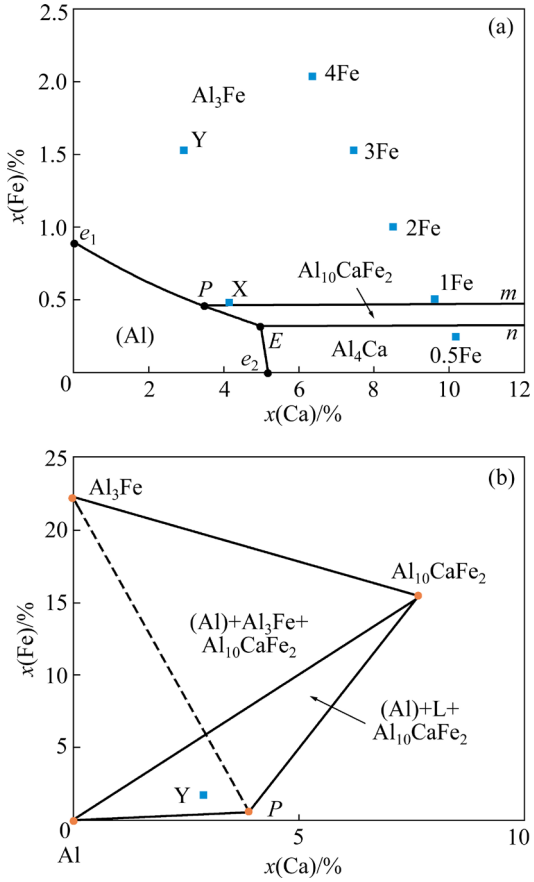

Fig. 12 Proposed liquidus (a) and peritectic quadrangle (b) of Al−Ca−Fe phase diagram in aluminum corner

calculated T_S values of all the experimental alloys are the same, i.e., 613 °C (Figs. 11(a−g)). This value is very close to the experimental one determined by the DSC method (Figs. 7(a−c)).

Generalization of experimental and calculated data allowed us to propose a liquidus projection and parameters of all invariant reactions of the Al−Ca−Fe system in the aluminum corner (Fig. 12(a) and Table 6). In particular, the calculated region of primary crystallization (Al) (i.e., the position of the lines e_1E and e_2E) agrees well with previously obtained experimental data [30]. The boundaries of the primary crystallization of intermetallic phases were determined based on the microstructure analysis of the hypereutectic alloys (see Fig. 3). The temperature of the invariant peritectic transformation L + Al_3Fe → (Al) + $Al_{10}CaFe_2$ was determined by the DSC method for the Y alloy. According to the heating curve (Fig. 6(b)) this temperature is 638 °C. Analysis of the microstructure of the Y alloy after exposure at temperatures above and below this value (Fig. 7) is consistent with the DSC results.

Table 6 Invariant reactions in aluminum corner of Al−Ca−Fe system

Point in Fig. 12(a)	Reaction	Composition of liquid/at.% (wt.%)		T/°C
		Ca	Fe	
e_1	L → (Al) + Al_3Fe	−	0.88 (1.8)	655
e_2	L → (Al) + Al_4Ca	5.25 (7.6)	−	617
E	L → (Al) + Al_4Ca+$Al_{10}CaFe_2$	4.99 (7.22)	0.32 (0.64)	613
P	L+ Al_3Fe → (Al) + $l_{10}CaFe_2$	3.3 (4.8)	0.5 (1.0)	638

The position of the Point P (Fig. 12(a) and Table 6) allows one to determine the position of the peritectic quadrangle Al_3Fe−Al−P−$Al_{10}CaFe$ determining the region of alloys in which the invariant peritectic transformation L + Al_3Fe → (Al) + $Al_{10}CaFe_2$ takes place. As can be seen from Fig. 12(b), the Y alloy falls into the triangle Al−P−$Al_{10}CaFe$ which is in this quadrangle region. This fact suggests that the peritectic transformation must end with the disappearance of the Al_3Fe phase. A quantitative assessment of the phases before and after this reaction shows that the amount of liquid upon the completion of this reaction should decrease significantly (from 83 wt.% to 64 wt.%), while the amount of aluminum, on the contrary, should increase (from 11 wt.% to 26 wt.%). This explains the significant thermal effects on the cooling curve (Fig. 6(b)).

The proposed structure of Al−Ca−Fe phase diagram in the aluminum corner allows one to analyze the reactions occurring in the experimental alloys, both in equilibrium and in nonequilibrium conditions. In particular, the monovariant peritectic transformation L + Al_3Fe → $Al_{10}CaFe_2$ (along the line nP) should take place in the 3Fe alloy after the formation of primary Al_3Fe crystals. The beginning of this reaction is traced on the DSC cooling curve (Fig. 6(a)) and in microstructure (Fig. 4). Under equilibrium conditions this reaction should result in the complete disappearance of the Al_3Fe phase and the formation of the $Al_{10}CaFe_2$ phase via the monovariant eutectic reaction L → Al_4Ca + $Al_{10}CaFe_2$ (along the line nE). However, the suppression of this reaction in real conditions leads to a deviation of the liquid phase composition from the equilibrium one and further solidification of the alloy continues in the field of the primary solidification of the binary Al_4Ca compound.

4.2 Microstructure of near-eutectic X alloy

The proposed structure of the Al−Ca−Fe phase diagram is consistent with the structure of the slowly solidified near eutectic X alloy, which is located close to the Point *P* (Fig. 12). Crystallization of this alloy begins with the formation of a small fraction of primary crystals of the ternary compound (Fig. 3(f), Fig. 5(a)) followed by the binary eutectic reaction L → (Al) + $Al_{10}CaFe_2$, corresponding to the line *PE*. As a result of this reaction, 2-phase (Al) + $Al_{10}CaFe_2$ colonies which contain iron in the bulk (Fig. 5(d)) are formed. The crystallization ends via the ternary eutectic reaction L → (Al) + Al_4Ca + $Al_{10}CaFe_2$ leading to the formation of the main structural component, i.e., 3-phase (Al) + Al_4Ca + $Al_{10}CaFe_2$ eutectic colonies containing the most part of calcium (Fig. 5(c)).

The proposed version of the Al−Ca−Fe phase diagram shows the possibility of complete binding of iron in an amount of up to 1% inclusively to the $Al_{10}CaFe_2$ compound, which has a more favorable morphology compared to most Fe-bearing phases. The crystal structure of this ternary compound and its composition (Table 4) allow one to calculate its density. The resulting value is 3.3 g/cm^3, which is less than that of compounds with a similar formula (Table 3).

From the proposed version of the Al−Ca−Fe phase diagram (Fig. 1 and Fig. 12), it is impossible to obtain a hypereutectic structure without primary crystals of binary intermetallic compounds using conventional casting techniques. Therefore, the most attractive alloys are near-eutectic ones, particularly the experimental X alloy. It is well-known that in many aluminum-based systems with an increase in the cooling rate during solidification, the primary crystallization region of (Al) expands in comparison with the equilibrium variant [2]. Since the cooling rate in the graphite mold is about 20 K/s, the structure of the X alloy is hypoeutectic and consists mainly of a colony of ternary eutectic (Al) + Al_4Ca + $Al_{10}CaFe_2$ (Fig. 2(f)).

The fine structure of the eutectic suggests the possibility of obtaining globular particles of intermetallic phases during annealing [2]. Fragmentation is detected at 500 °C (Fig. 13(a)),

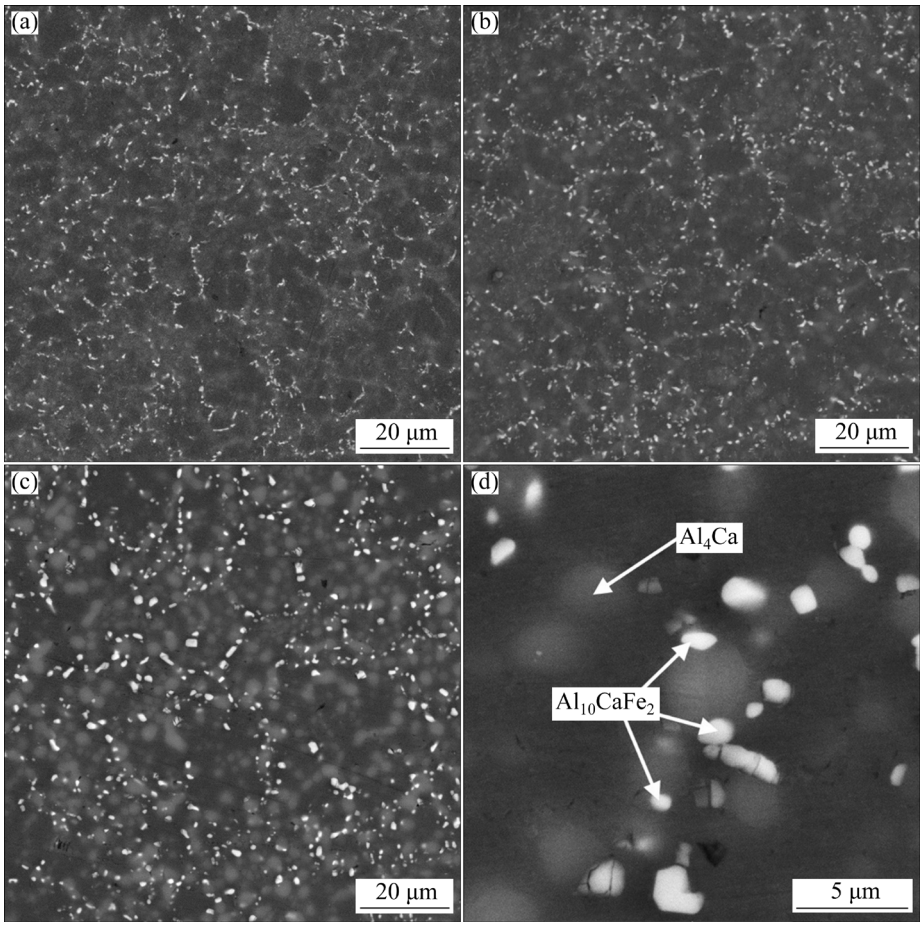

Fig. 13 SEM images of near-eutectic X alloy after annealing at 500 °C (a), 550 °C (b) and 600 °C (c, d) for 3 h

and at 550 °C the particles of both the Ca-containing phases acquire a globular shape (Fig. 13(b)). The high solidus temperature of the X alloy allows annealing at up to 600 °C. At this temperature, there is not only spheroidization, but also sufficiently strong coarsening (Fig. 13(c)). One should note that the particle size of the Al_4Ca phase is significantly larger compared to the ternary compound: ~2 and ~1 μm, respectively (Fig. 13(d)). Since the solubility of Ca and Fe in (Al) is negligible, the fractions of the phases in the X alloy can be calculated. In particular, they are 20.8 wt.% (23.4 vol.%) for the Al_4Ca phase and 4.1 wt.% (3.4 vol.%.) for the $Al_{10}CaFe_2$ phase. Thus, the total fraction of intermetallic particles is more than 25 vol.%, which is significantly larger than that in the aluminium alloys based on other eutectic systems, in particular (Al)+(Si) [1,2].

From the abovementioned results, one can see that the near-eutectic X alloy (Al−6wt.%Ca−1wt.%Fe) after annealing at 500−600 °C has a fine structure which is typical of aluminum matrix composites: globular particles of Al_4Ca and $Al_{10}CaFe_2$ phases (with a high volume fraction) uniformly distributed in the aluminum matrix.

5 Conclusions

(1) The phase diagram of the Al−Ca−Fe system in the aluminum corner, including the liquidus projection and solidification reactions, was studied by using the calculations and experimental methods. It is shown that in addition to the known binary phases (Al_3Fe and Al_4Ca), iron and calcium form a ternary compound whose composition corresponds to the formula $Al_{10}CaFe_2$.

(2) Two invariant reactions take place in this system: eutectic $L \rightarrow (Al) + Al_4Ca + Al_{10}CaFe_2$ (at 613 °C, 4.99 at.% Ca and 0.32 at.% Fe) and peritectic $L + Al_3Fe \rightarrow (Al) + Al_{10}CaFe_2$ (at 638 °C, 3.3 at.% Ca and 0.5 at.% Fe). Under the real solidification conditions, this peritectic transformation is not completed, and therefore crystals of the Al_3Fe phase are present in the as-cast structure.

(3) To assess the crystal lattice structure of the $Al_{10}CaFe_2$ phase, first principles calculations based on the density functional theory were carried out. Based on the calculations, data on the positions of the atoms and the shape of the unit cell corresponding to orthorhombic space group (*Cmcm*) and $YbFe_2Al_{10}$ structure type, and the lattice parameters (a=8.964 Å, b=10.174 Å, c=8.911 Å) were evaluated.

(4) The experimentally determined lattice parameters of the ternary compound (a=9.024 Å, b=10.200 Å, c=9.062 Å) formed during high temperature exposure at 620 °C of the Al−10.5wt.%Ca−3wt.%Fe alloy are proven to be quite close to the theoretically calculated values.

(5) It is shown that the Al−6wt.%Ca−1wt.%Fe near-eutectic alloy after annealing at 500−600 °C has a fine structure that is typical of aluminum matrix composites: globular particles of the Al_4Ca and $Al_{10}CaFe_2$ phases (with a total fraction of about 25 vol.%) uniformly distributed in aluminum. In this case, the size of the ternary compound particles is approximately 2 times smaller than that of the Al_4Ca phase.

CRediT authorship contribution statement

N. A. BELOV: Conceptualization, Supervision, Writing − Original draft, Visualization; **T. K. AKOPYAN:** Data curation, Writing − Review & editing, Resources, Methodology; **E. A. NAUMOVA:** Resources, Data curation; **V. V. DOROSHENKO:** Investigation, Data curation, Visualization; **T. A. SVIRIDOVA:** Data curation, Investigation, Visualization, Methodology; **N. O. KOROTKOVA:** Data curation, Investigation, Visualization.

Declaration of competing interest

The authors declare that they have no known competing financial interests or personal relationships that could have appeared to influence the work reported in this paper.

Acknowledgments

This work was financially supported by the Russian Science Foundation (No. 20-19-00746) (SEM, DSC, thermodynamic calculations), and the federal academic leadership program Priority 2030 of NUST MISIS (DFT, XRD).

References

[1] BELOV N A, AKOPYAN T K, NAUMOVA E A. Calcium-containing aluminum alloys [M]//Encyclopedia of Aluminum and Its Alloys [M]. London: CRC Press, Taylor & Francis Group, 2019.

[2] GLAZOFF M V, KHVAN A J, ZOLOTOREVSKIĬ V S, BELOV N A, DINSDALE A G. Casting aluminum alloys:

Their physical and mechanical metallurgy [M]. 2nd ed. London: Elsevier, 2018.

[3] NAUMOVA E, DOROSHENKO V, BARYKIN M, SVIRIDOVA T, LYASNIKOVA A, SHURKIN P. Hypereutectic Al−Ca−Mn−(Ni) alloys as natural eutectic composites [J]. Metals, 2021, 11: 890.

[4] NAUMOVA E A. Use of calcium in alloys: From modifying to alloying [J]. Russian Journal of Non-Ferrous Metals, 2018, 59(3): 284−298.

[5] BELOV N A, AKOPYAN T K, KOROTKOVA N O, NAUMOVA E A, PESIN A M, LETYAGIN N V. Structure and properties of Al−Ca(Fe, Si, Zr, Sc) wire alloy manufactured from as-cast billet [J]. JOM, 2020, 72(11): 3760−3768.

[6] SHURKIN P K, LETYAGIN N V, AKOPYAN T K, YAKUSHKOVA A I, SAMOSHINA M E, OZHERELKOV D Y, AKOPYAN T K. Remarkable thermal stability of the Al−Ca−Ni−Mn alloy manufactured by laser-powder bed fusion [J]. Materials Letters, 2021, 285: 129074.

[7] MONDOLFO L F. Aluminum alloys: Structure and properties [M]. London: Butterworths, 1976.

[8] KEVORKOV D, SCHMID-FETZER R. The Al−Ca system, Part 1: Experimental investigation of phase equilibria and crystal structures [J]. International Journal of Materials Research, 2022, 92: 946−952.

[9] OZTURK K, CHEN L Q, LIU Z K. Thermodynamic assessment of the Al−Ca binary system using random solution and associate models [J]. Journal of Alloys and Compounds, 2002, 340: 199−206.

[10] BELOV N A, DOROSHENKO V V, NAUMOVA E A, ILYUKHIN V D. Structure and mechanical properties of Al−6%Ca−1%Fe alloy foundry goods, obtained by die casting [J]. Tsvetnye Metally, 2017, 3: 69−75.

[11] ZHU L L, SOTO-MEDINA S, CUADRADO-CASTILLO W, HENNIG R G, MANUEL M V. New experimental studies on the phase diagram of the Al−Cu−Fe quasicrystal-forming system [J]. Materials & Design, 2020, 185: 108186.

[12] EZEMENAKA D, PHIRI A, KHVAN A, CHEVERIKIN V, FARTUSHNA I, DINSDALE A. An experimental investigation of phase transformations in the Al-rich corner of the Al−Cr−Fe system [J]. Journal of Alloys and Compounds, 2019, 808: 151692.

[13] ZHU L L, SOTO-MEDINA S, HENNIG R G, MANUEL M V. Experimental investigation of the Al−Co−Fe phase diagram over the whole composition range [J]. Journal of Alloys and Compounds, 2020, 815: 152110.

[14] JIANG L, RUAN Y, WEI B. Microstructural evolution and mechanical properties of ternary Al−Fe−Nb alloy under free fall condition [J]. Journal of Alloys and Compounds, 2020, 818: 153304.

[15] LIPPMANN S, KEMSIES R H, SCHICK M, MILKEREIT B, KESSLER O, RETTENMAYR M, HACK K. Synthesis of pure intermetallic phases on the example of the ternary phase τ1 in the system Al−Fe−Ni [J]. Intermetallics, 2019, 105: 107−112.

[16] BIAN Z, LIU Y, DAI S, CHEN Z, WANG M, CHEN D, WAN H. Regulating microstructures and mechanical properties of Al−Fe−Ni alloys [J]. Progress in Natural Science: Materials International, 2020, 30(1): 54−62.

[17] KAMAEVA L V, STERKHOVA I V, LAD'YANOV V I, RYLTSEV R E, CHTCHELKATCHEV N M. Phase selection and microstructure of slowly solidified Al−Cu−Fe alloys [J]. Journal of Crystal Growth, 2020, 531: 125318.

[18] GORNY A, MANICKARAJ J, CAI Z H, SHANKAR S. Evolution of Fe based intermetallic phases in Al−Si hypoeutectic casting alloys: Influence of the Si and Fe concentrations, and solidification rate [J]. Journal of Alloys and Compounds, 2013, 577: 103−124.

[19] ZHANG X Z, WANG D T, ZHOU Y X, CHONG X Y, LI X Z, ZHANG H T, NAGAUMI H. Exploring crystal structures, stability and mechanical properties of Fe, Mn-containing intermetallics in Al−Si Alloy by experiments and first-principles calculations [J]. Journal of Alloys and Compounds, 2021, 876: 160022.

[20] NOURI Z, TAGHIABADI R. Tribological properties improvement of conventionally-cast Al−8.5Fe−1.3V−1.7Si alloy by multi-pass friction stir processing [J]. Transactions of Nonferrous Metals Society of China, 2021, 31: 1262−1275.

[21] ENGİN S. Microstructure and mechanical properties of AlCuFe eutectic alloy [J]. Transactions of Nonferrous Metals Society of China, 2020, 30: 3183−3194.

[22] KRÁLÍK R, KŘIVSKÁ B, BAJTOŠOVÁ L, ŠLAPÁKOVÁ M, CIESLAR M. Homogenization of twin-roll cast AA8079 aluminum alloy studied by in-situ TEM [J]. Transactions of Nonferrous Metals Society of China, 2022, 32: 2138−2149.

[23] SONG D F, WANG S C, ZHAO Y L, LIU S H, DU Y, KANG Y H, WANG Z, ZHANG W W. Effect of melt holding on morphological evolution and sedimentation behavior of iron-rich intermetallic phases in Al−Si−Fe−Mn−Mg alloy [J]. Transactions of Nonferrous Metals Society of China, 2020, 30: 1−13.

[24] SHABESTARI S G. The effect of iron and manganese on the formation of intermetallic compounds in aluminum−silicon alloys [J]. Materials Science and Engineering: A, 2004, 383(2): 289−298.

[25] LU L, DAHLE A K. Iron-rich intermetallic phases and their role in casting defect formation in hypoeutectic Al−Si alloys [J]. Metallurgical and Materials Transactions A: Physical Metallurgy and Materials Science, 2005, 36(13): 819−835.

[26] KUCHARIKOVÁ L, TILLOVÁ E, BOKŮVKA O. Recycling and properties of recycled aluminium alloys used in the transportation industry [J]. Transport Problems, 2017, 11(2): 117−122.

[27] UTTARASAK K, CHONGCHITNAN W, MATSUDA K, CHAIRUANGSRI T, KAJORNCHAIYAKUL J, BANJONGPRASERT C. Evolution of Fe-containing intermetallic phases and abnormal grain growth in 6063 aluminum alloy during homogenization [J]. Results in Physics, 2019, 15: 102535.

[28] KUCHARIKOVÁ L, MAZUR M, TILLOVÁ E, CHALUPOVÁ M, ZÁVODSKÁ D, VAŠKO A. Fracture behavior of the secondary A226 cast alloy with 0.9% Fe [J]. Procedia Structural Integrity, 2018, 13: 1577−1582.

[29] LI Z D, LIMODIN N, TANDJAOUI A, QUAEGEBEUR P, WITZ J F, BALLOY D. Influence of Fe content on the damage mechanism in A319 aluminum alloy: Tensile tests and digital image correlation [J]. Engineering Fracture

Mechanics, 2017, 183: 94−108.
[30] BELOV N A, NAUMOVA E A, AKOPYAN T K, DOROSHENKO V V. Phase Diagram of the Al−Ca−Fe−Si system and its application for the design of aluminum matrix composites [J]. JOM, 2018, 70(11): 2710−2715.
[31] SHELEKHOV E V, SVIRIDOVA T A. Programs for X-ray analysis of polycrystals [J]. Metal Science and Heat Treatment, 2000, 42: 309−313.
[32] Thermo-Calc Software TTAL5 Al-Alloys. URL: www.thermocalc.com (accessed: 17.05.2021)
[33] GIANNOZZI P, BARONI S, BONINI N, et al. QUANTUM ESPRESSO: A modular and open-source software project for quantum simulations of materials [J]. Journal of Physics Condensed Matter, 2009, 21: 395502.
[34] GIANNOZZI P, ANDREUSSI O, BRUMME T, et al. Advanced capabilities for materials modelling with Quantum ESPRESSO [J]. Journal of Physics Condensed Matter, 2017, 29: 465901.
[35] URL: www.quantum-espresso.org/pseudopotentials (accessed: 10.06.2021)
[36] KALYCHAK Y M, BODAK O I, GLADYSHEVSKII E I. Ce−Mn−Ni system [J]. Soviet Physics, Crystallography, 1976, 21: 280−282.
[37] GLADYSHEVSKII E I, KRIPYAKEVICH P I, TESLYUK M Y, ZARECHNYUK O S, KUZ'MA Y B. Crystal structures of some intermetallic compounds [J]. Soviet Physics, Crystallography, 1961, 6(2): 267−268.
[38] GACZYŃSKI P, VAGIZOV F G, SUSKI W, KOTUR B, WOCHOWSKI K, DRULIS H. Magnetic properties and Möessbauer effect studies of $Ce_{1-x}Sc_xFe_4Al_8$ system [J]. Journal of Magnetism and Magnetic Materials, 2000, 214: 37−43.
[39] THIEDE V M T, EBEL T, JEITSCHKO W. Ternary aluminides LnT_2Al_{10} (Ln=Y, La-Nd, Sm, Gd-Lu and T=Fe, Ru, Os) with $YbFe_2Al_{10}$ type structure and magnetic-properties of the iron-containing series [J]. Journal of Materials Chemistry, 1998, 8(1): 125−130.
[40] YANSON T I, MANYAKO M B, BODAK O I, CERNY R, PACHECO J V, YVON K. Crystal structure of zirconium iron aluminide, Zr_6FeAl_2 [J]. Zeitschrift Für Kristallographie - New Crystal Structures, 1997, 212(1): 504.
[41] SCHOBINGER-PAPAMANTELLOS P, BUSCHOW K H J, RITTER C. Magnetic ordering and phase transitions of RFe_4Al_8 (R=La, Ce, Y, Lu) compounds by neutron diffraction [J]. Journal of Magnetism and Magnetic Materials, 1998, 186: 21−32.
[42] FELNER I, NOWIK I. Crystal structure magnetic properties and hyperfine interactions in RFe_4Al_8 (R=Rare Earth) systems [J]. Journal of Physics and Chemistry of Solids, 1978, 39: 951-956.
[43] MARKER M C J, SKOLYSZEWSKA-KÜHBERGER B, EFFENBERGER H S, SCHMETTERER C, RICHTER K W. Phase equilibria and structural investigations in the system Al−Fe−Si [J]. Intermetallics, 2011, 19(12): 1919−1929.

Al−Ca−Fe 合金中 $Al_{10}CaFe_2$ 化合物的形成与表征

N. A. BELOV[1], T. K. AKOPYAN[1,2], E. A. NAUMOVA[1],
V. V. DOROSHENKO[1], T. A. SVIRIDOVA[1], N. O. KOROTKOVA[1]

1. National University of Science and Technology MISIS, 4 Leninsky pr., Moscow 119049, Russia;
2. Baikov Institute of Metallurgy and Materials Science, 49 Leninsky pr., Moscow 119991, Russia

摘　要：采用热力学计算和实验技术研究铝角的 Al−Ca−Fe 体系相图，包括液相面投影图和凝固反应。结果表明，与铝固溶体(Al)平衡的不是 Al_3Fe 相，而是一种组成符合化学式 $Al_{10}CaFe_2$ 的三元化合物。通过包晶转变 $L + Al_3Fe \rightarrow (Al) + Al_{10}CaFe_2$ (638 ℃, 3.3% Ca 和 0.5% Fe, 摩尔分数)发生从二元化合物到三元化合物的转变。与针状 Al_3Fe 相夹杂物不同，三元化合物的初晶和共晶具有致密的形貌。使用第一性原理计算和 X 射线衍射分析确定三元化合物 $Al_{10}CaFe_2$ 的晶格结构。此外，近共晶合金 Al−6%Ca−1%Fe(质量分数)在 500~600 ℃退火后具有细晶组织，过量相的总体积分数约为 25%。因此，Al−Ca−Fe 体系可用于制造新的铝基复合合金。

关键词：Al−Ca 合金；金属间化合物；相图；相变；显微组织；铝基复合材料

(Edited by Xiang-qun LI)